

Static quantum dot on a potential hilltop for generating and analyzing hot electrons in the quantum Hall regime

Ryo Oishi,¹ Yuto Hongu,¹ Tokuro Hata,¹ Chaojing Lin,¹ Takafumi Akiho,² Koji Muraki,² and Toshimasa Fujisawa^{1,*}

¹*Department of Physics, Tokyo Institute of Technology,
2-12-1 Ookayama, Meguro, Tokyo, 152-8551, Japan.*

²*NTT Basic Research Laboratories, NTT Corporation,
3-1 Morinosato-Wakamiya, Atsugi 243-0198, Japan.*

(Dated: September 12, 2024)

We propose and demonstrate a static quantum dot on a potential hilltop to generate and analyze ballistic hot electrons along a quantum Hall edge channel well above the chemical potential. High energy resolution associated with discrete energy levels is attractive for studying hot-electron dynamics. Particularly, the energy distribution function of hot electrons weakly coupled to cold electrons is investigated to reveal spectral diffusion with energy relaxation. The analysis allows us to estimate the maximum energy exchange per scattering, which is an important parameter to describe interacting electrons in the edge channel.

I. INTRODUCTION

Ballistic hot-electron transport in the quantum Hall regime is attractive for studying electron dynamics and developing electronic quantum optics with flying electrons, where highly non-equilibrium hot (high-energy) electrons are spatially and energetically separated from cold (low-energy) electrons near the chemical potential [1–3]. The crossed electric and magnetic fields induce long ballistic transport over a millimeter along a potential contour, when the scattering processes, such as LO phonon emission and Coulomb interaction with cold electrons, are well suppressed [4–7]. Such ballistic transport can be seen by exciting electrons well above the chemical potential typically by 30 – 100 meV [8]. Unlike photons, a strong anti-bunching correlation of two hot electrons has been identified as a result of Coulomb repulsion, which can be used for designing non-linear functionality [9, 10]. Such hot-electron dynamics are often studied with dynamic quantum dots (QDs), by which a single hot electron is generated dynamically on-demand by applying rapid voltage pulses [11–14]. In contrast, a single potential barrier is widely used as an energy spectrometer, which has an energy resolution of only a few meV for typical GaAs heterostructures [8, 10]. Quantum-dot energy spectrometers with discrete energy levels are highly desirable for higher energy resolution, which would allow us to distinguish coherent transport from others and identify otherwise hidden inelastic processes. However, typical QDs with multiple electrons work only at low energies close to the chemical potential and cannot be used as a hot-electron spectrometer [15, 16].

Here, we demonstrate that a single static QD can be used for generating and detecting hot electrons with a high energy resolution by preparing an empty QD on a potential hilltop. Such a hilltop QD has Coulomb charging energy and discrete energy spacing comparable to

those of conventional QDs for cold electrons. We find that hot electrons injected from a point contact have an asymmetric energy distribution with a sharp Fermi edge on the high-energy side and a broadened tail on the low-energy side. When hot electrons are allowed to interact even weakly with cold electrons, the hot electrons relax, accompanied by spectral diffusion, in agreement with the numerical simulation of electron-electron scattering. The relation between the relaxation and the spectral diffusion can be used to extract the maximum energy exchange per scattering in the edge channel.

II. HILLTOP QD

Figure 1(a) schematically shows how a QD is defined at the top of a potential hill that separates two regions of different chemical potentials (labeled B and R, which stand for base and reference, respectively). The electrochemical potential ε_1 for the first electron in the QD is located close to the chemical potential μ_R (defined to be $\mu_R = 0$) of the right region but much higher than that $\mu_B = -eV_B$ (< 0) of the base region with large bias voltage V_B (> 0). When ε_1 is slightly below μ_R , hot electrons with energy ε_1 can be injected into the base with a narrow spectral width, as shown by the energy distribution function f_h in the inset. The injected hot electrons are well isolated from cold electrons in the base. The hilltop QD works as a narrow-band hot-electron injector under this condition.

When ε_1 is made slightly above μ_R , as shown in Fig. 1(b), hot electrons traveling to the right in the base can be analyzed with the level ε_1 of the QD. To test this scheme, hot electrons are injected through a point contact (PC) from the emitter region (labeled E) with the chemical potential $\mu_E = +eV_E$ (> 0) and voltage $-V_E$ ($V_E > 0$). The initial energy distribution function has a high-energy cutoff at μ_E and a broad low-energy tail due to the weak energy dependence of the tunneling probability, as shown in the inset (i). This sharp cutoff, which

* fujisawa@phys.titech.ac.jp

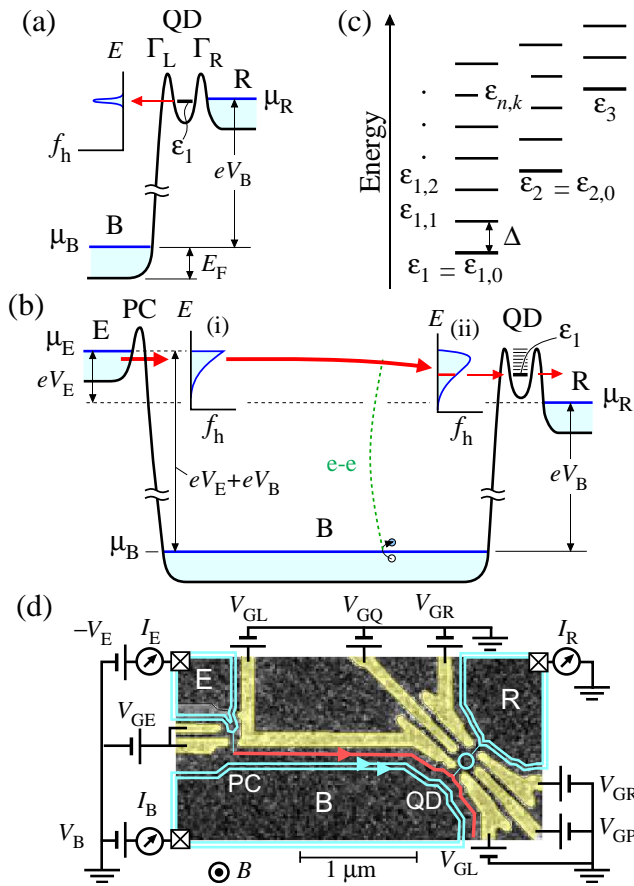


FIG. 1. (a) Energy diagram of a QD on a large potential hilltop between the base (B) and the right reference (R) channels. A hot electron can be injected from the electrochemical potential ε_1 for the first electron in the QD. The inset shows the energy distribution function of the injected hot electrons. (b) Energy diagram for analyzing hot electrons emitted from the emitter (E) through a point contact (PC). The insets (i) and (ii) show the energy distribution functions of hot electrons just after the injection and after electron-electron scattering, respectively. (c) Energy diagram of electrochemical potential $\varepsilon_{n,k}$ for the k -th n -electron state. Transport through n -electron ground state is associated with ε_n ($\equiv \varepsilon_{n,k}$). (d) Schematic measurement setup with a false-color scanning electron micrograph of a control sample. The cyan lines represent the cold edge channels, and the red line shows the potential contour where ballistic hot electrons travel. The polarity of the voltage on the emitter is intentionally reversed to express the initial hot-electron energy as $(eV_E + eV_B)$ in the base.

should be determined by the base temperature T_B of the system (the emitter region), can be used to evaluate the spectroscopic resolution of the hilltop QD. If the hot electrons scatter with cold electrons in the base, the energy distribution function at the analyzer broadens, as shown in the inset (ii). Such electron-electron (e-e) scattering can be investigated with a hilltop QD by changing the scattering rate with V_B while keeping all other settings

of the emitter and spectrometer the same.

For these purposes, an empty hilltop QD has to be prepared with no permanently occupied electrons. This is not a difficult task, because excess electrons will escape from the QD to the base. Generally, ε_1 ($\equiv \varepsilon_{1,0}$) for the first electron is the lowest one of electrochemical potential $\varepsilon_{n,k}$ for k -th electronic state ($k = 0, 1, 2, \dots$ from the ground state) of n -electron QD ($n = 1, 2, 3, \dots$), as shown in Fig. 1(c). Even when the hot-electron energy distribution is significantly broader than the level spacing $\Delta = \varepsilon_{1,1} - \varepsilon_{1,0}$ of the QD, the spectroscopic analysis can be performed dominantly with the lowest level ε_1 , as shown in the following experiment.

Such a hilltop QD was formed in a standard modulation-doped AlGaAs/GaAs heterostructure with a two-dimensional electron system (2DES) located 100 nm below the surface. As shown in Fig. 1(d), a PC and a QD can be formed with split gates in the same design as the device used in Ref. [17]. All measurements were performed at the electron temperature of $T_B \simeq 100$ mK (comparable to the lattice temperature). A magnetic field of 3.8 T was applied perpendicular to the 2DES with electron density of $1.7 \times 10^{11} \text{ cm}^{-2}$ and low-temperature mobility of about $10^6 \text{ cm}^2/\text{Vs}$. The electrons occupy the Landau levels with the filling factor $\nu = 2$ in the bulk, and chiral edge channels are formed as shown by the cyan lines, although integer filling is not required for this experiment. At $\nu = 2$, the Fermi level E_F of the edge state measured from the lowest Landau level in the bulk should be about half the cyclotron energy, 3 meV at 3.8 T. Under appropriate bias voltages of V_B ($= 0 - 100$ mV) and V_E ($= 0 - 15$ mV), gate voltages V_{Gm} on gate Gm with $m = E, L, P, Q$, and R were adjusted to form a hilltop QD and a PC separated by a distance of $L = 2 \mu\text{m}$. Hot electrons injected from the emitter to the base will propagate along the potential contour (the red line). The currents I_E , I_B , and I_R at the emitter, base, and reference regions, respectively are simultaneously measured. See Appendix A and B for the quantum Hall effect and potential profile of the device, respectively.

Standard Coulomb blockade oscillations with isolated current peaks in I_R are seen at small V_B , as shown in Fig. 2(a) for $V_B = 0.1$ mV, where the two gate voltages V_{GL} and V_{GR} are swept at $V_{GP} = V_{GQ} = -300$ mV. The current peak appears when the n -electron chemical potential ε_n ($\equiv \varepsilon_{n,0}$) is located between μ_R and μ_B . When V_B is made slightly greater than the charging energy E_C (about 2 meV) of the QD, the peaks are broadened and partially overlapped, as shown in Fig. 2(b) for $V_B = 3$ mV. While the current is out of the range of the ammeter in the hatched region, the Coulomb oscillations are visible as periodic kinks (marked by the red lines) at $\varepsilon_n = \mu_R$ along the boundary of the conductive region. For both cases, the tunneling rates Γ_L and Γ_R of the left and right barriers are primarily controlled by the gate voltages V_{GL} and V_{GR} , respectively, and thus the current vanishes if either Γ_L or Γ_R becomes lower than the measurement limit ($\Gamma_{\text{lim}} \sim 1$ MHz for 160 fA). Therefore, the last peak in

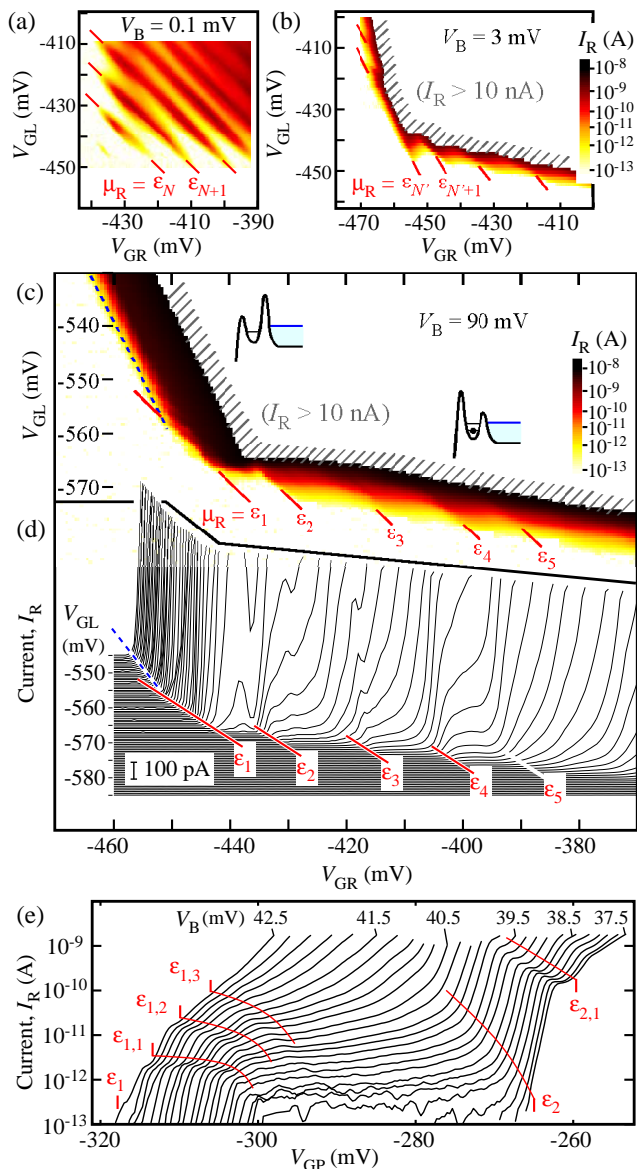


FIG. 2. (a) Standard Coulomb blockade oscillations in the current I_R measured at low bias $V_B = 0.1$ mV. (b) Partially overlapped Coulomb oscillations at $V_B = 3$ mV greater than the charging energy of about 2 meV. (c and d) Coulomb oscillations of the hilltop QD at large $V_B = 90$ mV in the color scale plot (c) and the linear line plot (d) of the same data. Each line in (d) is offset for clarity. (e) Current steps in I_R as a function of the plunger gate voltage V_{GP} for various V_B . The peak, kink, and step structures in (a-e) are associated with electrochemical potentials ε_n ($\equiv \varepsilon_{n,0}$) and $\varepsilon_{n,k}$ of the QD.

Fig. 2(a) and the last kink in Fig. 2(b) seen at the lower left end of the conductive region should be determined by this measurement limit, not by emptying the QD.

The condition to form the hilltop QD for the first electron can be found by sweeping V_{GL} and V_{GR} under a large V_B , as shown in the color plot of Fig. 2(c) and the line

plot of Fig. 2(d) for the same data set taken at $V_B = 90$ mV. Because the left barrier is electrostatically influenced by the large V_B , large negative $V_{GL} \simeq -570$ mV is needed to pinch off the channel. The conductive region is terminated by the left smooth boundary and periodic kinks along the bottom boundary. The period of the kinks is comparable to those in Fig. 2(a) and (b), which suggests that the kinks are related to the Coulomb oscillations at $\varepsilon_n = \mu_R$ of the hilltop QD. The current profiles in Fig. 2(d) show clear Coulomb staircases around the kinks [18]. The staircases appear only along the bottom boundary, where the left barrier is higher ($\Gamma_L \ll \Gamma_R$) and electrons can accumulate in the QD [the energy diagram shown in the right inset to Fig. 2(c)]. In contrast, the QD should be fully emptied in the opposite limit, $\Gamma_L \gg \Gamma_R$, along the left boundary (left inset), which explains the absence of kinks along the left boundary. Namely, the left boundary marked by the blue dashed line should be determined by the measurable limit for the right barrier ($\Gamma_R \sim \Gamma_{lim}$) with the QD empty. Under this condition, the QD states do not contribute to the transport. Therefore, the last kink at the lower left corner of the conductive region should be attributed to the transport through the first electron state of the QD at $\varepsilon_1 = \mu_R$ with comparable tunneling rates $\Gamma_L \sim \Gamma_R$. One can use this condition for generating and detecting hot electrons in the base.

Discrete energy levels in the hilltop QD can be resolved in the fine sweep of plunger gate voltage V_{GP} , as shown in Fig. 2(e). Here, the current profile is obtained at various V_B values and fixed $V_{GL} = -0.5$ V and $V_{GR} = -0.453$ V. Between the large current onsets for the first electron at $\mu_R = \varepsilon_1$ and the second electron at ε_2 , step-wise features marked by the red lines are observed. These current steps are attributed to the excited states at $\varepsilon_{1,k}$. By using the lever arm factor $\alpha = 0.055$ for V_{GP} estimated from the following measurement, we obtained the onsite charging energy $E_C = \varepsilon_2 - \varepsilon_1 = 1.8$ meV and the level spacing $\Delta = \varepsilon_{1,1} - \varepsilon_1 = 0.2$ meV. These values are comparable to those for a conventional QD with a similar device structure [17, 19–21].

For our electrostatically-defined QD, the overall current decreases with decreasing V_B , which can be understood by considering that the left barrier height is increased with decreasing V_B (See Appendix C for the relation to the Coulomb diamond characteristics). It should be noted that the current steps associated with the discrete levels are not clearly seen for small $V_B < 39$ mV. This can be understood by considering the competition between energy relaxation within and escape from the QD. If Γ_L is much greater than the relaxation rate Γ_{rel} , electrons in the QD excited levels will escape before relaxing to the ground state, where the current reflects the state-dependent Γ_L . For example, the data at $V_B > 42$ mV suggests that Γ_L for the first excited state is about 10 times greater than Γ_L for the ground state. For $\Gamma_L \ll \Gamma_{rel}$, on the other hand, electrons in the excited state will relax to the ground state before escaping [22]. This explains why the current remains constant in the

range of $\varepsilon_1 < \mu_R < \varepsilon_2$ for the data at $V_B < 39$ mV. In this range, the hilltop QD can be used as a hot-electron injector with a tunable kinetic energy $eV_B - (\mu_R - \varepsilon_1)$ in the base. The injected electrons should have a narrow spectral width comparable to the transition width from the zero current to the constant current (about $20 \mu\text{eV}$ for the present data). Ideally, the width can be reduced to the lifetime broadening $\hbar\Gamma_L$ ($\approx 0.004 \mu\text{eV}$ for 1 pA). Such a monochromatic hot-electron source is attractive for studying hot-electron dynamics.

III. ENERGY SPECTROSCOPY FOR HOT ELECTRONS

A. QD spectrometer

We apply this hilltop QD as a spectrometer to investigate ballistic hot-electrons injected from a point contact (PC), as shown in Fig. 1(b). The hot-electron energy distribution function $f_h(\varepsilon)$, which describes the occupation probability $0 \leq f_h \leq 1$ for a state at energy ε , can be measured with the hilltop QD at $\varepsilon_1 > 0$, where only one-electron states with $\varepsilon_{1,k}$ contribute to the transport. If the energy distribution is narrower than the level spacing Δ of the QD, the current I_R is proportional to $\Gamma^{(1,k)} f_h(\varepsilon_{1,k})$ for the transport through the k -th state with the overall tunneling rate $\Gamma^{(1,k)}$. $f_h(\varepsilon)$ can be measured directly from the $\varepsilon_{1,k}$ dependence of I_R . In our experiment using a PC as the injector, the distribution is much wider than Δ . Therefore, the current $I_R \propto \sum_k \Gamma^{(1,k)} f_h(\varepsilon_{1,k})$ is contributed by a multiple of one-electron states k . If $\varepsilon_{1,k}$ is equally spaced from the minimum ε_1 , and if $\Gamma^{(1,k)}$ is independent of the states, the current can be approximated to be $I_R \propto \int_{\varepsilon_1}^{\infty} f_h(\varepsilon) d\varepsilon$. In this case, the distribution function $f_h(\varepsilon) \propto -\frac{d}{d\varepsilon_1} I_R$ can be obtained from the derivative of I_R with respect to ε_1 . The validity of the scheme is discussed with experimental data, as shown below.

In the experiment, the emitter voltage $-V_E$ ($V_E = 0 - 15$ mV) is applied relative to the reference electrode, and thus the injected hot electron has maximum kinetic energy $E_{EB} = eV_E + eV_B$ in the base. The hot electrons are injected with constant current $I_E = 1$ nA by tuning the emitter gate voltage V_{GE} with a feedback program after setting all experimental conditions (V_E , V_{GL} , V_{GR} , V_{GP} , etc.). For this small I_E , we assume that spin-up electrons in the emitter enter the lowest Landau level in the base. Because the hot-electron distribution function should be small ($f_h \lesssim 0.01$) for this I_E , we adjusted the gate voltages for the QD to yield large tunneling rates Γ_L and Γ_R to obtain sufficiently large detector current in I_R . Under the hot electron injection, the QD current I_R is measured as a function of V_{GL} and V_{GR} , as shown in the inset to Fig. 3(a). In addition to the positive I_R due to electron escape from the QD to the base, which is accompanied by Coulomb oscillations with kinks (the red lines), we ob-

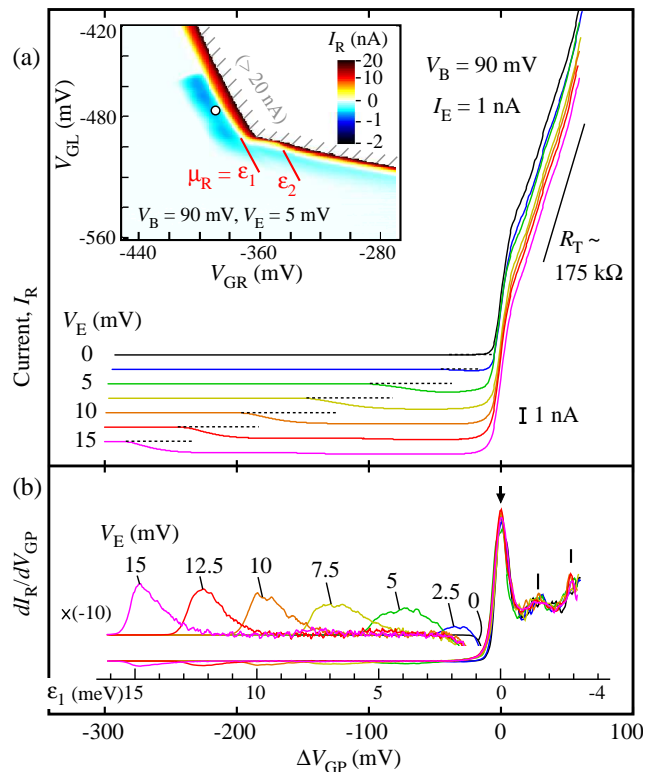


FIG. 3. (a) Current I_R as a function of the plunger gate voltage ΔV_{GP} taken at several V_E values. Each line is offset for clarity. The dashed lines represent the zero level ($I_R = 0$). The inset shows the color scale plot of I_R obtained by a two-dimensional sweep of V_{GL} and V_{GR} . The QD condition for the main panel is marked by the circle in the inset. (b) dI_R/dV_{GP} for the data in (a). Sign-reversed magnified plots [$\times(-10)$] are also shown. The horizontal axis ΔV_{GP} is measured from the largest peak in dI_R/dV_{GP} and is converted to $\varepsilon_1 = -\Delta V_{GP}$ as shown in the inset scale.

serve in some regions negative I_R (the blue region), which is a manifestation of hot electrons entering the QD. Large negative I_R appears near the last kink at $\mu_R \lesssim \varepsilon_1$ for the first electron. This is the situation where the hilltop QD can probe the hot electrons. In contrast, small negative I_R is seen along the bottom boundary (the blue region at $V_{GR} > -360$ mV), where multiple electrons contribute to the transport. No negative current is seen along the left boundary ($V_{GL} > -460$ mV), where the well-defined QD may not have formed. These characteristics ensure that the hot electrons are primarily detected with one-electron QD states in the large-negative- I_R region ($V_{GR} < -380$ mV and $V_{GL} < -460$ mV). See Appendix D for further discussions on the hot-electron detection. The following measurements were performed in the middle of the large-negative- I_R region marked by the circle, where the two barriers are expected to have comparable tunneling rates ($\Gamma_L \approx \Gamma_R$).

The energy spectroscopy was performed by measuring I_R as a function of V_{GP} , as shown in the main plot of

Fig. 3(a). Its derivative dI_R/dV_{GP} is shown in Fig. 3(b). The largest current step in positive I_R (the largest peak marked by the arrow in dI_R/dV_{GP}) is attributed to the resonance at $\mu_R = \varepsilon_1$, and thus the horizontal axis ΔV_{GP} was defined by the shift of V_{GP} from the resonant condition. The energy scale for $\varepsilon_1 = -\alpha\Delta V_{GP}$ is also shown in Fig. 3(b) by assuming a linear shift of ε_1 with $\alpha = 0.055$. Before analyzing the hot electron spectroscopy, we examine the QD characteristics seen in the positive- I_R region. In Fig. 3(a), I_R increases almost linearly with ε_1 , which suggests a tunneling resistance of $R_T = 175$ k Ω including the series resistance in the setup. Under this high tunneling conductance R_T^{-1} , discrete levels of the QD are unresolved even in the dI_R/dV_{GP} traces in Fig. 3(b). The peaks in dI_R/dV_{GP} at $\Delta V_{GP} \simeq 0, 30$ and 52 meV (marked by the vertical bars) seems to be associated with the charging energy (about 1.5 meV) of the QD. The large peak at $\Delta V_{GP} = 0$ could be enhanced by the Fermi edge singularity [23, 24]. If we neglect the peak structures, dI_R/dV_{GP} at $\Delta V_{GP} > 0$ is almost constant in agreement with the Fermi distribution function and the constant density of edge states. This supports that the proposed scheme with $f_h(\varepsilon) \propto \frac{d}{d\varepsilon_1} I_R$ works for this highly-conductive QD. Whereas we did not resolve discrete levels here, the overall tunneling rate $\Gamma^{(1,k)}$ can be regarded as a constant in this energy regime. The scheme should work even better for hot electrons, as many-body effects should be absent for sparse electrons ($f_h \ll 1$).

For the data at $\Delta V_{GP} < 0$ in Fig. 3(a), the hot electrons yield a negative current $I_R \simeq -0.8$ nA comparable in amplitude to $I_E = 1$ nA, which suggests that the QD is quite transparent above ε_1 . The negative current disappears at large negative ΔV_{GP} . The vanishing point [the peak position in the magnified $-dI_R/dV_{GP}$ plot of Fig. 3(b)] shifts almost linearly with increasing V_E , which supports the linear energy shift of $\varepsilon_1 = -\alpha\Delta V_{GP}$ for this energy range. A small deviation from linearity (not clear in this plot) will be discussed later in connection with relaxation. Therefore, $-dI_R/dV_{GP}$ as a function of ΔV_{GP} can be viewed as a distribution function $f_h(\varepsilon_1)$. The distribution function is asymmetrically broadened particularly at large $V_E = 15$ mV.

The broadening is clearly seen in the logarithmic plot of $-dI_R/dV_{GP}$ as a function of ε_1 in Fig. 4(a) for the data taken at different V_B values. Here, the relative energy between the emitter and the detector is fixed at $V_E = 11$ meV to keep the same emitter-detector configuration. The spectral change with V_B can be explained by the electron-electron scattering. As illustrated in Fig. 4(b), the scattering is reduced by increasing the physical distance between hot and cold electrons at larger V_B [8, 19]. Importantly, all spectra are terminated at $\varepsilon_1 \simeq \mu_E = 11$ meV. The observation of the high-energy cutoff at μ_E ensures that a fraction of electrons transport ballistically over a distance $L = 2$ μm . For $\varepsilon_1 > \mu_E$, $-dI_R/dV_{GP}$ decays exponentially as $e^{-\varepsilon_1/\rho}$ with $\rho \simeq 0.2$ meV at $V_B = 90$ mV. Considering that the thermal energy ($k_B T_B \simeq 10$ μeV) of the emitter is much smaller than ρ , ρ should be

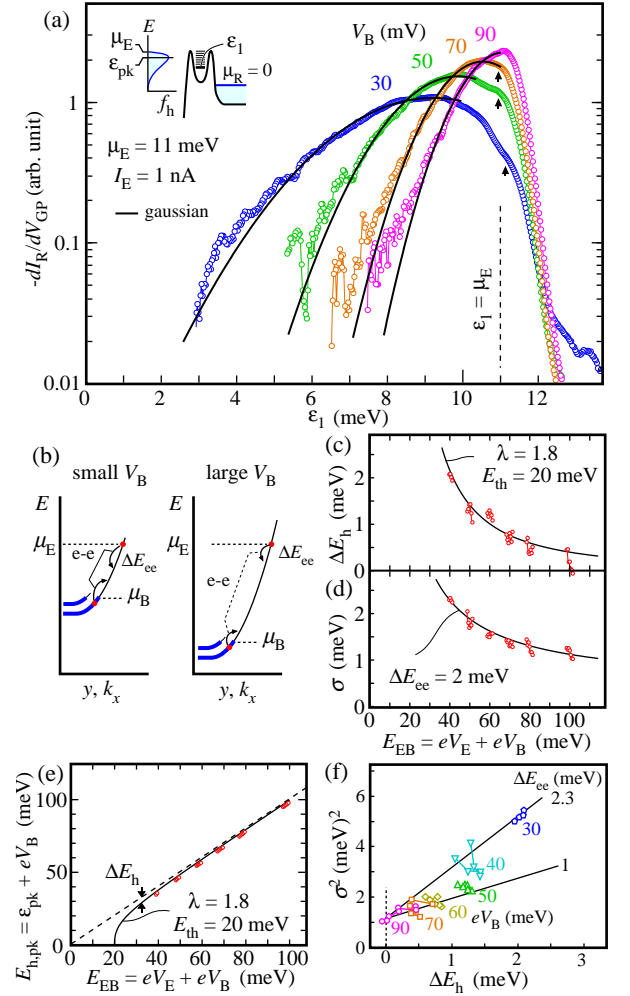


FIG. 4. (a) Measured $-dI_R/dV_{GP}$ (the circles) taken at several V_B values as a function of ε_1 converted from V_{GP} . The profile can be regarded as the distribution function $f_h(\varepsilon_1)$. The dashed line for $\varepsilon_1 = \mu_E$ ($= 11$ meV) represents the high-energy cutoff by the emitter chemical potential. The low-energy profile on the left side of the peak was fitted with a Gaussian function (the black solid lines) with the peak position ε_{pk} and the standard deviation σ . The inset shows the energy diagram of the measurement. (b) Energy (E) - momentum (k_x) dispersion relations of the edge channels at small and large V_B . The e-e scattering with maximum energy exchange ΔE_{ee} is shown. (c) The energy loss $\Delta E_h = eV_E - \varepsilon_{pk}$, (d) σ , and (e) the peak energy $E_{h,pk} = \varepsilon_{pk} + eV_B$ as a function of the energy bias $E_{EB} = eV_E + eV_B$. The solid lines in (c-e) are based on the empirical model with parameters $\lambda = 1.8$, $E_{th} = 20$ meV, and $\Delta E_{ee} = 2$ meV (see text). (f) σ^2 as a function of ΔE_h to estimate ΔE_{ee} from the slope.

determined by the resolution of the highly transparent QD.

In contrast, the spectra at $\varepsilon_1 < \mu_E$ are significantly broadened. The spectrum taken at $V_B = 90$ mV shows a peak position close to μ_E , which suggests negligible e-e scattering. With decreasing V_B , the peak is shifted to the

low-energy side. As all spectra are asymmetric around the peak, the low-energy side of the peak is fitted by a Gaussian function, as shown by the black curves, from which the peak position ε_{pk} and the standard deviation σ are obtained. The energy loss $\Delta E_{\text{h}} = eV_{\text{E}} - \varepsilon_{\text{pk}}$ and the broadening σ are obtained for various conditions, as summarized in Fig. 4(c) and (d) with fine tuning of $V_{\text{E}} = 5 - 11$ mV (connected by the red lines) and coarse tuning of $V_{\text{B}} = 40 - 90$ meV in the step of 10 mV. They are plotted as a function of the excitation energy $E_{\text{EB}} = eV_{\text{E}} + eV_{\text{B}}$ in the base. Generally, both ΔE_{h} and σ decrease with increasing E_{EB} , which can be understood by the reduction of e-e scattering, because the hot electrons are spatially separated from the cold electrons in the base. While ΔE_{h} approaches to zero at $E_{\text{EB}} \gtrsim 100$ meV, finite $\sigma \sim 1$ meV remains. This residual σ should be related to the energy dependence of the tunneling probability of the emitter PC.

Previously, the relation between the initial and final energy after traveling a finite distance has been investigated by using point-contact spectroscopy [8]. This relation can be tested using the hilltop QD with higher energy resolution. We plot the initial energy E_{EB} and final energy $E_{\text{h,pk}} = \varepsilon_{\text{pk}} + eV_{\text{B}}$ at $L = 2$ μm , as shown in Fig. 4(e). The lever arm factor $\alpha = 0.0547$ was determined to make this plot so that $E_{\text{h,pk}}$ calculated with $\varepsilon_{\text{pk}} = -\alpha e\Delta V_{\text{GP,pk}}$ from the peak position $\Delta V_{\text{GP,pk}}$ in ΔV_{GP} asymptotically approaches the ballistic condition (the dashed line) at large E_{EB} . Whereas the deviation from the ballistic condition is not clear in this plot, finite deviation ΔE_{h} is identified with the high-resolution QD spectrometer, as shown in Fig. 4(c).

Generally, hot electrons can also be scattered by emitting LO phonons and tunneling into other Landau levels. Such unwanted processes should induce additional signals well separated from the ballistic signal by the LO phonon energy (about 36 meV) and the cyclotron energy (about 6 meV) [8]. Because we focused on the narrow energy range around the ballistic condition, the present analysis is made only for the hot electrons that have not experienced these processes. Since we obtain a large signal ($|I_{\text{R}}/I_{\text{E}}| \simeq 0.8$), the unwanted processes should play minor roles in the present analysis.

B. e-e scattering

The measurement of distribution functions allows us to characterize the e-e scattering process in detail. The scattering can be characterized by two parameters; the maximum energy exchange ΔE_{ee} per scattering due to the non-momentum-conserving scattering and the effective interaction strength γ per length [see Eq. (9) in Ref. [25]]. Particularly, ΔE_{ee} is the important parameter that distinguishes the single-particle excitations ($E > \Delta E_{\text{ee}}$) and many-body excitations ($E < \Delta E_{\text{ee}}$) for excitation energy E . We have previously estimated ΔE_{ee} by measuring the electron-hole excitation near the Fermi energy

[19]. Here, we estimate ΔE_{ee} from the hot-electron distribution function and provide a complementary data set.

We employ the single-particle scattering approach shown in Ref. [25, 26]. Whereas $\Delta E_{\text{ee}} \ll k_{\text{B}}T_{\text{B}}$ was assumed there, we used $\Delta E_{\text{ee}} \gg k_{\text{B}}T_{\text{B}}$ in the following analysis, because $\Delta E_{\text{ee}} > 0.5$ meV (much greater than $k_{\text{B}}T_{\text{B}} \simeq 10$ μeV) was suggested from the electron-hole excitation [19]. By assuming $f_{\text{h}}(E) \ll 1$, the master equation for spatial (x) evolution of $f_{\text{h}}(E; x)$ reads

$$\frac{\partial}{\partial x} f_{\text{h}}(E; x) = \gamma \int_0^{\infty} d\epsilon e^{-\left(\frac{\epsilon}{\Delta E_{\text{ee}}}\right)^2} D_{\text{c}}(\epsilon) [f_{\text{h}}(E + \epsilon; x) - f_{\text{h}}(E; x)], \quad (1)$$

where the scattering from energy $E + \epsilon$ to E with the energy loss ϵ (> 0) is suppressed by the factor $e^{-\left(\frac{\epsilon}{\Delta E_{\text{ee}}}\right)^2}$ with parameter ΔE_{ee} . Here, $D_{\text{c}}(\epsilon) = \int_{-\infty}^{\infty} dE f_{\text{c}}(E - \epsilon) [1 - f_{\text{c}}(E)]$ is the density of electron-hole excitation of cold electrons with the distribution function $f_{\text{c}}(E)$ and is approximated to be $D_{\text{c}}(\epsilon) = \epsilon$ for $\epsilon \geq 0$ and 0 for $\epsilon \leq 0$ at low temperature ($T_{\text{B}} = 0$).

In the present case, the initial distribution function is expected to be $f_{\text{h}}(E; 0) = f_0 \exp\left(\frac{E - \mu_{\text{E}}}{w}\right)$ with an exponential decay for $E \leq \mu_{\text{E}}$ and $f_{\text{h}}(E; 0) = 0$ with a sharp cut off for $E > \mu_{\text{E}}$. f_0 ($\ll 1$) is a constant that depends on the emitter current $I_{\text{E}} = \frac{e}{h} \int_{-\infty}^{\infty} f_{\text{h}}(E; 0) dE$. The spatial evolution $f_{\text{h}}(E; x)$ can be obtained by integrating Eq. (1), as shown in Fig. 5(a) calculated with $w = 1$ meV and $\Delta E_{\text{ee}} = 1$ meV. The initial function is transformed toward a Gaussian-like function. Interestingly, the sharp peak at $E = \mu_{\text{E}}$ remains visible even if the ballistic signal $f_{\text{h}}(\mu_{\text{E}}; x)$ is heavily attenuated by the scattering, because scattering with small energy loss ($\epsilon \simeq 0$) is suppressed by the factor $D_{\text{c}}(\epsilon)$. This ballistic signal can be smeared out if the detector energy resolution is not sufficiently high. We consider an energy window function $g(E) = \frac{1}{\sqrt{2\pi}\rho} \exp\left(-\frac{E^2}{2\rho^2}\right)$ to describe the energy resolution of width ρ , and the measurement yields a convolution $\tilde{f}_{\text{h}}(E) = (f_{\text{h}} * g)(E)$ of $f_{\text{h}}(E)$ and $g(E)$. The convoluted $\tilde{f}_{\text{h}}(E; x)$ with $\rho = 0.2$ meV is shown in Fig. 5(b), which qualitatively reproduces the relaxation and broadening of the experimental data in Fig. 4(a). Interestingly, the signature of the ballistic transport is seen as the small bumps marked by the vertical bars at $E = \mu_{\text{E}}$ in Fig. 5(b) and probably by the arrows at $\varepsilon_1 = \mu_{\text{E}}$ in Fig. 4(a). The similarity implies that 10 - 60 % of detected electrons have transported ballistically over $L = 2$ μm for $V_{\text{B}} = 30 - 90$ meV.

For comparison, the same simulation is performed with $\Delta E_{\text{ee}} = 2$ meV in Fig. 5(c) showing more broadening, and $\Delta E_{\text{ee}} = 0.5$ meV in Fig. 5(d) showing less broadening. Here, the range of γx values for each ΔE_{ee} is chosen to yield comparable peak shifts by using the scaling $[\gamma x \propto (\Delta E_{\text{ee}})^{-3}]$. The simulation indicates that γ and ΔE_{ee} can be determined from the peak shift and the broadening. Crude comparison with the data suggests

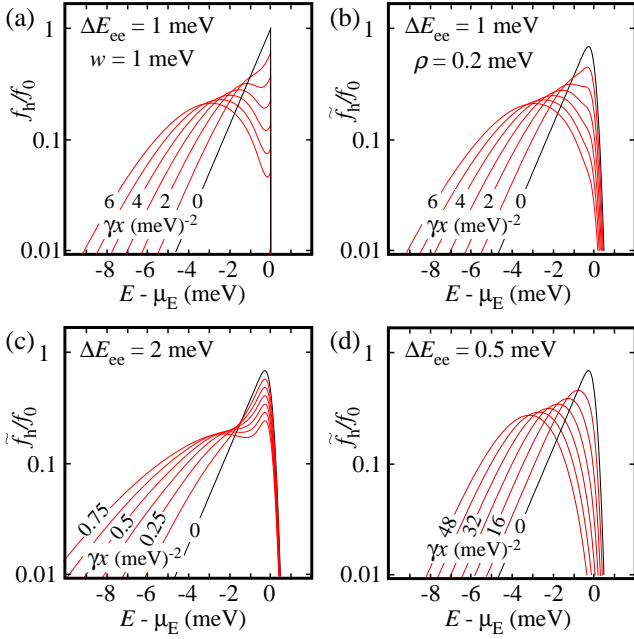


FIG. 5. (a) Calculated evolution of the energy distribution function $f_h(E)$ of hot electrons injected from an emitter with chemical potential μ_E . (b-d) Expected evolution of convoluted distribution function $\tilde{f}_h(E) = (f_h * g)(E)$ with an energy window function $g(E)$ with width $\rho = 0.2$ meV. The maximum energy exchange per scattering is $\Delta E_{ee} = 1$ meV in (a) and (b), 2 meV in (c), and 0.5 meV in (d). The black trace in each panel shows the initial function with $w = 1$ meV.

$\Delta E_{ee} \sim 1$ meV in our sample.

Since our measurement was performed at a fixed distance $L = 2 \mu\text{m}$, the spectroscopic change with V_B in Fig. 4(a) suggests variations of γ and/or ΔE_{ee} with V_B . To evaluate the parameters, we expand $f_h(E + \epsilon) \simeq f_h(E) + \epsilon \frac{\partial}{\partial E} f_h(E) + \frac{1}{2} \epsilon^2 \frac{\partial^2}{\partial E^2} f_h(E)$ up to the second order of E to derive a Fokker-Planck equation of the form

$$\frac{\partial}{\partial x} f_h(E; x) = \eta \left[\frac{\partial}{\partial E} f_h(E) + \frac{\Delta E_{ee}}{\sqrt{\pi}} \frac{\partial^2}{\partial E^2} f_h(E) \right] \quad (2)$$

from Eq. (1). Here, $\eta \equiv \frac{\sqrt{\pi}}{4} \gamma (\Delta E_{ee})^3$ describes the energy-relaxation velocity $\eta = \frac{d}{dx} \langle E \rangle$. By assuming a Gaussian form of the solution

$$f_h(E; x) = \frac{f_0}{\sqrt{2\pi}\sigma} \exp \left[-\frac{(E - \langle E \rangle)^2}{2\sigma^2} \right], \quad (3)$$

the average energy $\langle E(x) \rangle = \langle E_0 \rangle - \eta x$ and the standard deviation $\sigma(x) = \sqrt{\sigma_0^2 + \frac{2}{\sqrt{\pi}} \eta \Delta E_{ee} x}$ changes with x from the initial values $\langle E_0 \rangle$ and σ_0 . Therefore, $\eta = \Delta E_h/L$ ($= 0 - 1$ meV/ μm) can be obtained from the energy loss ΔE_h in Fig. 4(c). ΔE_{ee} can be estimated from the combined relation

$$\sigma^2 = \sigma_0^2 + \frac{2}{\sqrt{\pi}} \Delta E_{ee} \Delta E_h, \quad (4)$$

i.e., the slope of the $\sigma^2 - \Delta E_h$ plot in Fig. 4(f). ΔE_{ee} has a weak energy dependence; about 1 meV at $E > 50$ meV and 2.3 meV at $E \sim 30$ meV, in good agreement with our previous work (about 1 meV at $E = 50$ meV and 2 meV at $E = 30$ meV in Fig. 9 of Ref [19]). The coincidence with different measurement schemes justifies the proposed scheme and ensures the obtained parameter.

The energy dependence of ΔE_{ee} can be understood with the concave edge potential profile, which can be regarded as the one-dimensional energy E - momentum k_x relation, as shown in Fig. 4(b). For non-linear dispersion, e-e scattering must be accompanied by a finite change in the total momentum, which is allowed in the presence of random impurity potential. The maximum momentum change Δk_x , which is related to the correlation length of the impurity potential, induces the maximum energy exchange $\Delta E_{ee} = \hbar |v_c^{-1} - v_h^{-1}|^{-1} \Delta k_x$. Here, v_h and v_c are the drift velocities $v = \frac{1}{\hbar} \frac{d}{dk_x} E$ for hot and cold electrons, respectively. This qualitatively explains why ΔE_{ee} increases with decreasing the hot-electron energy.

The initial-energy (E_{EB}) dependence of $E_{h,pk}$ in Fig. 4(e) as well as ΔE_h in Fig. 4(c) can be understood by phenomenological energy dependence of $\eta \propto E^{-\lambda}$, where the power λ ($= 0.5 \sim 4$) depends on the details of the edge potential profile, the screening effect from the metal gate, and the velocity of the cold electrons in the base [8]. $\lambda = 2$ is suggested for non-interacting cold electrons and negligible screening effect. This empirical power law is convenient as it provides an analytical solution of $\frac{d}{dx} \langle E \rangle = \eta$. For initial average energy $\langle E_0 \rangle$, $\langle E(L) \rangle$ at $x = L$ is given by

$$\langle E(L) \rangle = \left[\langle E_0 \rangle^{1+\lambda} - E_{th}^{1+\lambda} \right]^{\frac{1}{1+\lambda}} \quad (5)$$

with parameters λ and E_{th} . By regarding E_{EB} as $\langle E_0 \rangle$ and $E_{h,pk}$ as $\langle E(L) \rangle$ in Fig. 4(e), the experimental data can be reproduced with Eq. (5), as shown by the solid line with $\lambda = 1.8$ and $E_{th} = 20$ meV. These values are comparable to those in the previous study [8, 19]. Moreover, the σ data in Fig. 4(d) can be reproduced with Eq. (4), where a constant $\Delta E_{ee} = 2$ meV was used for simplicity as its energy dependence is not precisely determined in this experiment. In this way, the relaxation dynamics of hot electrons is successfully investigated with the hilltop QD.

IV. SUMMARY

In summary, we developed a hilltop QD to generate and analyze hot electrons whose energy is well above the chemical potential of cold electrons. Taking advantage of discrete energy levels in the QD, the scheme can be used as a high-energy-resolution emitter and spectrometer. We applied this technique to resolve the asymmetric energy distribution function of hot electrons injected from the emitter. The distribution is significantly

broadened by Coulomb interaction with cold electrons. The analysis with a master equation characterizes the energy loss and the broadening with some parameters. The developed hilltop QD can be used to study ballistic hot-electron transport in various ways. Whereas the QD spectroscopy was demonstrated with high tunneling conductance in this experiment, the resolution can be improved further by making the tunneling rates smaller. As suggested in this experiment, the hilltop QD can be used as a hot-electron emitter with a narrow spectral width to launch a spatially broadened wave packet. If required, the hilltop QD can be driven with a voltage pulse to launch a hot electron on demand and to detect hot electrons in a time-resolved fashion [27–29]. The present scheme should be useful in studying ballistic hot electron transport.

Acknowledgements

This study was supported by the Grants-in-Aid for Scientific Research (KAKENHI JP19H05603, JP23K17302, JP24K00552, and JP24H00827) and "Advanced Research Infrastructure for Materials and Nanotechnology in Japan (ARIM)" of the Ministry of Education, Culture, Sports, Science and Technology (MEXT).

Appendix A: Quantum Hall effect

The quantum Hall effect of the device used in this study is shown in the Hall resistance R_{xy} and the longitudinal resistance R_{xx} of Fig. S1, where all gate voltages were set to zero. Whereas the ohmic contacts and the conductive region of the device are not designed for a standard Hall bar, clear quantized Hall conductance in R_{xy} and zero longitudinal resistance in R_{xx} are resolved in some magnetic-field regions including $B = 3.8$ T where the measurement in the main paper was performed.

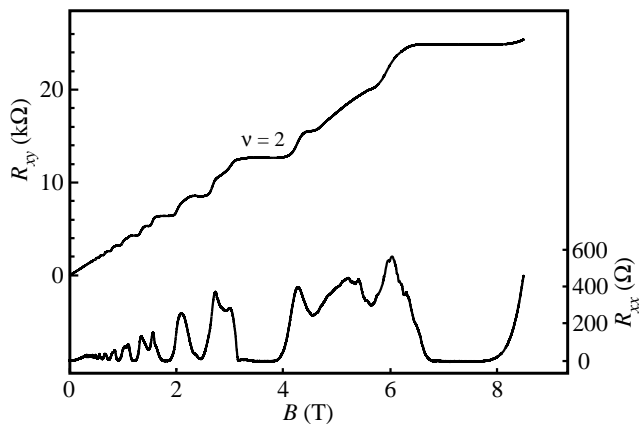


FIG. S 1. The Hall resistance R_{xy} and the longitudinal resistance R_{xx} as a function of the magnetic field B .

Appendix B: Potential profile

It may be useful to see the potential profile for a better understanding of the device characteristics. Figure S2 shows a schematic potential profile of the device for analyzing hot electrons injected from a point contact (PC) with a hilltop quantum dot (QD). This potential profile was obtained by calculating the electrostatic potential at 100 nm below the surface, where the two-dimensional electron system (2DES) should exist, under a given surface potential profile [30]. The surface potentials in the gated and ungated regions are chosen for illustration purposes. For simplicity, we neglected the potential induced by the charges of the 2DES and donors. While the profile should be regarded as a schematic, one can see how the PC and QD can be formed at the tops of the potential hill from the base side.

With the grounded reference electrode labeled R with chemical potential $\mu_R = 0$, slightly larger chemical potential $\mu_E = eV_E (> 0)$ is set to the emitter labeled E, and large negative potential $\mu_B = -eV_B (< 0)$ is applied to the base labeled B. The 2DESs in the emitter, base, and reference regions are shown by cyan color and corresponding edge channels (only for spin-up) are shown by the blue lines. Hot electrons injected from the PC into the base have significantly large kinetic energy as compared to cold electrons in the edge channels of the base. The hot electrons propagate along the equipotential line (the red line) based on the drift motion under the crossed electric and magnetic fields. The hot electrons may experience electron-electron (e-e) scattering during the propagation. The scattering strength depends on the physical distance between hot and cold electrons and can be reduced by increasing V_B , as shown in the main paper. The energy distribution function of hot electrons is investigated by using the hilltop QD.

As discussed in the main text, e-e scattering is sensitive to the edge potential primarily determined by the base potential μ_B and the gate voltage V_{GL} . V_{GL} has to be sufficiently negative to define the transport path of hot electrons but not too much negative to suppress

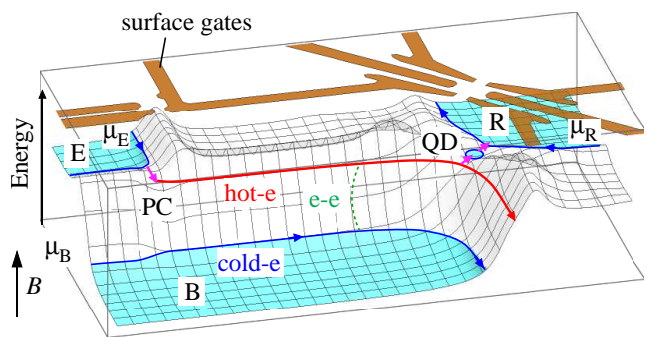


FIG. S 2. Schematic potential profile of the device and the surface gate pattern.

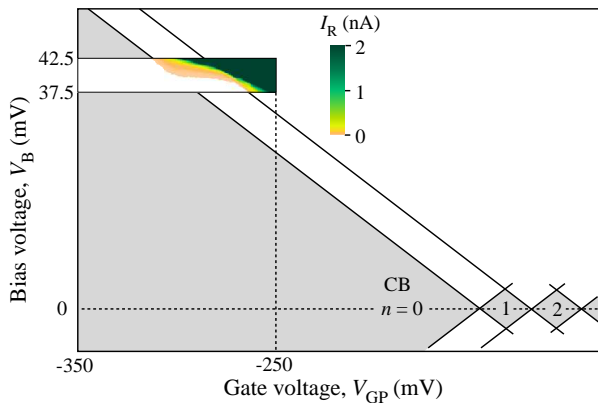


FIG. S 3. Schematic charging diagram of the QD in the $V_{GP} - V_B$ plane. CB regions are shown in gray. A color plot of I_R [the same data as in Fig. 2(e)] is attached.

unwanted processes like LO phonon scattering and inter-Landau-level scattering, because these processes become efficient if the edge potential is steeper.

Appendix C: Coulomb diamond

While Coulomb diamond characteristics are widely investigated for conventional QDs, we do not observe clear Coulomb diamond for the hilltop QD. Figure S3 shows schematic Coulomb diamond characteristics when the gate voltage V_{GP} and the bias voltage V_B are swept in the wide range. The Coulomb blockade regions for electron number $n = 1, 2, \dots$ appear as diamond patterns in this diagram, and the maximum bias voltage within the Coulomb blockade condition is determined by the charging energy of the QD. For the demonstrated hot-electron spectroscopy, we utilize the semi-infinitely wide Coulomb blockade region of the empty QD ($n = 0$), where the bias voltage can exceed the charging energy.

The current I_R shown in Fig. 2(e) is attached to Fig. S3 as a color-scale plot, where the onsets for $n = 1$ and 2 transport regions are adjusted to the schematic charging diagram. Because the voltage V_B on the base strongly influences the left tunneling barrier of the QD, the current level changes drastically with V_B . Therefore, the onsets for $n = 1$ and 2 are visible only in the limited regions. It is not an easy task to observe the entire Coulomb diamond characteristics in a single $V_B - V_{GP}$ scan. In this

study, every time V_B is changed, we swept V_{GL} and V_{GR} to find the condition for the last kink, as shown in Fig. 2(c) for example at $V_B = 90$ mV.

Appendix D: Hot-electron detection

A color plot of the current I_R shown in the inset to Fig. 3(a) is shown as line plots in Fig. S4, where the current onsets for $n = 1$ ($\mu_R = \varepsilon_1$) and 2 ($\mu_R = \varepsilon_2$) are highlighted by the red lines. Other onsets for $n \geq 3$ are smeared out because we adjusted the $n = 1$ QD highly conductive (still in the tunneling regime) to obtain sufficient detector current, and thus the dot for $n > 2$ may not be formed in the tunneling regime. Because the negative I_R is seen in the vicinity of the last onset along $\mu_R = \varepsilon_1$, the QD should play an essential role in the detection.

However, several features cannot be explained with the simple model. For instance, the maximum detector current is very high ($I_R = -0.8$ nA close to $I_E = 1$ nA in amplitude) in the wide region near the last onset $\mu_R \leq \varepsilon_1$ in Fig. S4. We need further studies to investigate how the hilltop QD efficiently carries hot electrons.

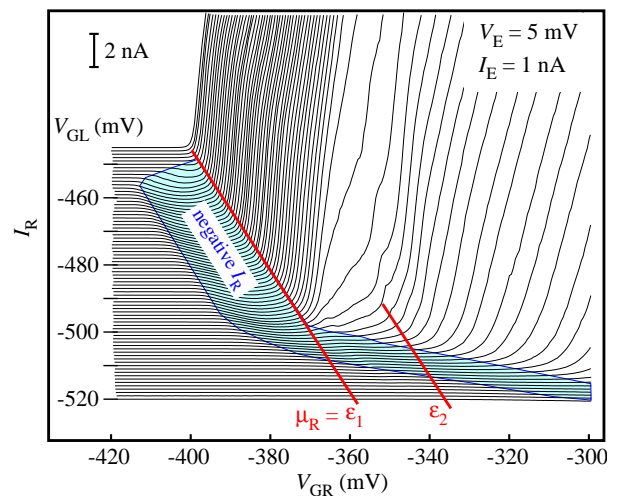


FIG. S 4. Line plots of I_R as a function of V_{GR} for different V_{GL} . Each line is offset for clarity.

- [1] C. Bäuerle, D. C. Glattli, T. Meunier, F. Portier, P. Roche, P. Roulleau, S. Takada and X. Waintal, Coherent control of single electrons: a review of current progress, Rep. Prog. Phys. **81**, 056503 (2018).
- [2] H. Edlbauer, J. Wang, T. Crozes, P. Perrier, S. Ouacel, C. Geffroy, G. Georgiou, E. Chatzikiyiakou, A. Lacerda-

Santos, X. Waintal, D. C. Glattli, P. Roulleau, J. Nath, M. Kataoka, J. Spletstoesser, M. Acciai, M. C. da Silva Figueira, K. Oztas, A. Trellakis, T. Grange, O. M. Yevtushenko, S. Birner and C. Bauerle, Semiconductor-based electron flying qubits: review on recent progress accelerated by numerical modelling, EPJ Quantum Tech-

- nology 9, 21 (2022).
- [3] Z. F. Ezawa, *Quantum Hall Effects: Recent Theoretical and Experimental Developments*, 3rd edition, (World Scientific, Singapore, 2013).
- [4] D. Taubert, C. Tomaras, G. J. Schinner, H. P. Tranitz, W. Wegscheider, S. Kehrein, and S. Ludwig, Relaxation of hot electrons in a degenerate two-dimensional electron system: Transition to one-dimensional scattering, *Phys. Rev. B* **83**, 235404 (2011).
- [5] N. Johnson, C. Emary, S. Ryu, H.-S. Sim, P. See, J. D. Fletcher, J. P. Griffiths, G. A. C. Jones, I. Farrer, D. A. Ritchie, M. Pepper, T. J. B. M. Janssen, and M. Kataoka, LO-phonon emission rate of hot electrons from an on demand single-electron source in a GaAs/AlGaAs heterostructure, *Phys. Rev. Lett.* **121**, 137703 (2018).
- [6] S. Akiyama, T. Hirasawa, Y. Sato, T. Akiho, K. Muraki, and T. Fujisawa, Ballistic hot-electron transport in a quantum Hall edge channel defined by a double gate, *Appl. Phys. Lett.* **115**, 243106 (2019).
- [7] C. Emary, L. A. Clark, M. Kataoka, and N. Johnson, Energy relaxation in hot electron quantum optics via acoustic and optical phonon emission, *Phys. Rev. B* **99**, 045306 (2019).
- [8] T. Ota, S. Akiyama, M. Hashisaka, K. Muraki, and T. Fujisawa, Spectroscopic study on hot-electron transport in a quantum Hall edge channel, *Phys. Rev. B* **99**, 085310 (2019).
- [9] N. Ubbelohde, L. Freise, E. Pavlovskaya, P. G. Silvestrov, P. Recher, M. Kokkalis, G. Barinovsky, F. Hohls, T. Weimann, K. Pierz and V. Kashcheyevs, Two electrons interacting at a mesoscopic beam splitter, *Nat. Nanotechnol.* **18**, 733 (2023).
- [10] J. D. Fletcher, W. Park, S. Ryu, P. See, J. P. Griffiths, G. A. C. Jones, I. Farrer, D. A. Ritchie, H. S. Sim and M. Kataoka, Time-resolved Coulomb collision of single electrons, *Nat. Nanotechnol.* **18**, 727 (2023).
- [11] M. Kataoka, N. Johnson, C. Emary, P. See, J. P. Griffiths, G. A. C. Jones, I. Farrer, D. A. Ritchie, M. Pepper, and T. J. B. M. Janssen, Time-of-flight measurements of single-electron wave packets in quantum Hall edge states, *Phys. Rev. Lett.* **116**, 126803 (2016).
- [12] J. D. Fletcher, P. See, H. Howe, M. Pepper, S. P. Giblin, J. P. Griffiths, G. A. C. Jones, I. Farrer, D. A. Ritchie, T. J. B. M. Janssen, and M. Kataoka, Clock-controlled emission of single-electron wave packets in a solid-state circuit, *Phys. Rev. Lett.* **111**, 216807 (2013).
- [13] N. Ubbelohde, F. Hohls, V. Kashcheyevs, T. Wagner, L. Fricke, B. Kaestner, K. Pierz, H. W. Schumacher, and R. Haug, Partitioning of on-demand electron pairs, *Nature Nanotech.* **10**, 46 (2014).
- [14] J. D. Fletcher, N. Johnson, E. Locane, P. See, J. P. Griffiths, I. Farrer, D. A. Ritchie, P. W. Brouwer, V. Kashcheyevs, and M. Kataoka, Continuous-variable tomography of solitary electrons, *Nature Commun.* **10**, 5298 (2019).
- [15] C. Altimiras, H. le Sueur, U. Gennser, A. Cavanna, D. Mailly, and F. Pierre, Non-equilibrium edge-channel spectroscopy in the integer quantum Hall regime. *Nat. Phys.* **6**, 34 (2010).
- [16] H. le Sueur, C. Altimiras, U. Gennser, A. Cavanna, D. Mailly, and F. Pierre, Energy Relaxation in the Integer Quantum Hall Regime, *Phys. Rev. Lett.* **105**, 056803 (2010).
- [17] R. Konuma, C.J. Lin, T. Hata, T. Hirasawa, T. Akiho, K. Muraki, and T. Fujisawa, Nonuniform heat redistribution among multiple channels in the integer quantum Hall regime, *Phys. Rev. B* **105**, 235302 (2022).
- [18] T. Ihn, 'Semiconductor Nanostructures: Quantum States and Electronic Transport', Oxford Univ. Press (2010).
- [19] K. Suzuki, T. Hata, Y. Sato, T. Akiho, K. Muraki and T. Fujisawa, Non-thermal Tomonaga-Luttinger liquid eventually emerging from hot electrons in the quantum Hall regime, *Commun. Phys.* **6**, 103 (2023).
- [20] K. Washio, R. Nakazawa, M. Hashisaka, K. Muraki, Y. Tokura, and T. Fujisawa, Long-lived binary tunneling spectrum in the quantum Hall Tomonaga-Luttinger liquid, *Phys. Rev. B* **93**, 075304 (2016).
- [21] K. Itoh, R. Nakazawa, T. Ota, M. Hashisaka, K. Muraki and T. Fujisawa, Signatures of a Nonthermal Metastable State in Copropagating Quantum Hall Edge Channels. *Phys. Rev. Lett.* **120**, 197701 (2018).
- [22] T. Fujisawa, D. G. Austing, Y. Tokura, Y. Hirayama, S. Tarucha, Electrical pulse measurement, inelastic relaxation, and non-equilibrium transport in a quantum dot, *J. Physics: Cond. Matt.(Topical Review)* **15**, R1395 (2003).
- [23] K. Tobias, C. Livio, R. Christian, W. Werner, G. Leonid, I. Thomas, and E. Klaus, Fermi edge singularities in transport through lateral GaAs quantum dots, *New J. Phys.* **19**, 023009 (2017).
- [24] A. S. Goremykina and E. V. Sukhorukov, Fermi-edge singularity and related interaction induced phenomena in multilevel quantum dots, *Phys Rev B* **95**, 155419 (2017).
- [25] A. M. Lunde and S. E. Nigg, Statistical theory of relaxation of high-energy electrons in quantum Hall edge states, *Phys. Rev. B* **94**, 045409 (2016).
- [26] A. M. Lunde, S. E. Nigg and M. Büttiker, Interaction-induced edge channel equilibration, *Phys. Rev. B* **81**, 041311 (2010).
- [27] H. Kamata, N. Kumada, M. Hashisaka, K. Muraki, and T. Fujisawa, Fractionalized wave packets from an artificial Tomonaga-Luttinger liquid. *Nat. Nanotech.* **9**, 177 (2014).
- [28] M. Hashisaka, N. Hiyama, T. Akiho, K. Muraki, and T. Fujisawa, Waveform measurement of charge- and spin-density wavepackets in a chiral Tomonaga-Luttinger liquid, *Nat. Phys.* **13**, 559 (2017).
- [29] C.J. Lin, M. Hashisaka, T. Akiho, K. Muraki, T. Fujisawa, Quantized charge fractionalization at quantum Hall Y junctions in the disorder-dominated regime, *Nat. Commun.* **12**, 131 (2021).
- [30] J. H. Davies, I. A. Larkin, and E. V. Sukhorukov, Modeling the patterned two-dimensional electron gas: Electrostatics, *J. Appl. Phys.* **77**, 4504 (1995).